
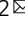



# A four-electron Zn-I<sub>2</sub> aqueous battery enabled by reversible I<sup>-</sup>/I<sub>2</sub>/I<sup>+</sup> conversion

Yiping Zou<sup>1</sup>, Tingting Liu<sup>1</sup>, Qijun Du<sup>1</sup>, Yingying Li<sup>1</sup>, Haibo Yi<sup>1</sup>, Xing Zhou<sup>1</sup>, Zhuxin Li<sup>1</sup>, Lujie Gao<sup>1</sup>, Lan Zhang<sup>1</sup> & Xiao Liang<sup>1,2</sup>  

Electrochemically reversible redox couples that embrace more electron transfer at a higher potential are the eternal target for energy storage batteries. Here, we report a four-electron aqueous zinc-iodine battery by activating the highly reversible I<sub>2</sub>/I<sup>+</sup> couple (1.83 V vs. Zn/Zn<sup>2+</sup>) in addition to the typical I<sup>-</sup>/I<sub>2</sub> couple (1.29 V). This is achieved by intensive solvation of the aqueous electrolyte to yield ICl inter-halogens and to suspend its hydrolysis. Experimental characterization and modelling reveal that limited water activity and sufficient free chloride ions in the electrolyte are crucial for the four-electron process. The merits of the electrolyte also afford to stabilize Zn anode, leading to a reliable Zn-I<sub>2</sub> aqueous battery of 6000 cycles. Owing to high operational voltage and capacity, energy density up to 750 Wh kg<sup>-1</sup> based on iodine mass was achieved (15–20 wt% iodine in electrode). It pushes the Zn-I<sub>2</sub> battery to a superior level among these available aqueous batteries.

<sup>1</sup>State Key Laboratory of Chem/Bio-Sensing and Chemometrics, College of Chemistry and Chemical Engineering, Hunan University, Changsha 410082, P.R. China. <sup>2</sup>Advanced Catalytic Engineering Research Center of the Ministry of Education, Hunan University, Changsha 410082, P.R. China. email: [xliang@hnu.edu.cn](mailto:xliang@hnu.edu.cn)

The ever-increasing demands from portable electronic devices, electric vehicles, and renewable energy sources call for safe, low-cost storage batteries of high energy density<sup>1</sup>. One approach is to extend state-of-the-art Li-ion batteries to new rocking-chair systems with earth-abundant charge carriers, such as Na<sup>+</sup>, K<sup>+</sup>, Ca<sup>2+</sup>, Mg<sup>2+</sup>, Zn<sup>2+</sup>, Al<sup>3+</sup> ions<sup>2–6</sup>. The potential of using the metal anode instead of the insertion host further promises high energy density. Nonetheless, most of these systems involve organic solvents as the electrolyte, facing intrinsic safety issues in terms of flammability or leakage hazards for large-scale applications. The use of the aqueous solution as the electrolyte, however, has excluded most of the earth-abundant metal anodes. Zinc metal holds a specific capacity of 820 mAh g<sup>-1</sup>, is particularly promising as the anode for the aqueous batteries<sup>7</sup>. Another approach is exploiting multivalent conversion type cathodes, for example, sulfur and oxygen with high specific capacity<sup>8,9</sup>. Though promising, they are challenged by the intrinsic instability of the intermediates product, namely, the polysulfide shuttle and the peroxide/superoxide attack in Li-S and Li/Na-O<sub>2</sub> batteries<sup>10,11</sup>, respectively. In brief, we believe that developing safe, low-cost and high energy density batteries requires an aqueous system that integrates the metal anode and the multivalent conversion cathode.

The cathode for the aqueous zinc-ion batteries is intensively studied recently, including the intercalation metal oxide frameworks and the conversion type halogens<sup>12</sup>. The metal oxides, mainly the layered MnO<sub>2</sub><sup>13</sup> and V<sub>2</sub>O<sub>5</sub><sup>14</sup>, are plagued by sluggish intercalation/de-intercalation kinetics because of the large electron density of the Zn<sup>2+</sup> ions thus only limited rate capability and low capacity could be delivered. The halogens, on the other hand, are soluble in electrolyte solvent thus have fast conversion kinetics, as exemplified by the Zn-I<sub>2</sub><sup>15,16</sup> and Zn-Br<sup>17</sup> batteries. It also benefits their applications in organic metal batteries, such as Li-I<sub>2</sub>, Na-I<sub>2</sub>, K-I<sub>2</sub> to Mg-I<sub>2</sub>, and Al-I<sub>2</sub> batteries<sup>18–22</sup>. A recent report of a stimulus-responsive Zn-I<sub>2</sub> battery with overcharge self-protection function achieved by employing a smart pH-responsive electrolyte, solved the substantial safety concern and extends the lifespan of the Zn-I<sub>2</sub> batteries<sup>23</sup>. These halogen batteries share similar reversible conversion between X<sup>-</sup> and X<sub>2</sub>/X<sub>3</sub><sup>-</sup> (X = Cl, Br and I), however, they fail to fully make the advantages of the high energy density of the metal anodes due to the single electron transfer per halogen ion (or two electrons per halogen). Another recent study managed to intercalate Br<sup>o</sup> and Cl<sup>o</sup> into graphite, offering a brilliant concept for designing a high-energy and safe battery<sup>24</sup>. Previous studies<sup>25–28</sup> attempt to use high-valence iodine like IO<sub>4</sub><sup>-</sup>/IO<sub>3</sub><sup>-</sup> involving an attractive multi-electrons conversion upon redox in the battery. Although acidic electrolyte and heavy metal salts of the oxy acid of iodine<sup>27,29</sup> were introduced to enhance the stability of cathode<sup>30</sup>, a reversible battery is yet to be developed. Moreover, the acidic electrolyte decomposes the zinc anode due to severe hydrogen evolution.

In this work, we report a four-electron transfer aqueous zinc-iodine battery by activating the highly reversible I<sub>2</sub>/I<sup>+</sup> couple in addition to the typical I<sup>-</sup>/I<sub>2</sub> couple, which doubles the capacity of the conventional iodine batteries. Both experimental characterization and modeling reveal that the new redox couple is correlated to the electrolyte coordination structure: (1) decrease the H<sub>2</sub>O activity of the electrolyte solution by intensive ion coordination to suppress the detrimental hydrolysis of I<sup>+</sup> species; (2) promote the population of the free chloride ions with higher mobility thus facilitate the I<sub>2</sub>/I<sup>+</sup> redox kinetics by the formation of ICl inter-halogens. The well-defined two voltage profile of iodine chemistry in the deliberated bisalt electrolyte—holding a theoretical capacity of 422 mAh g<sup>-1</sup> assume four-electron conversion—delivers a capacity of 594 mAh g<sup>-1</sup> by combining the double layer capacitor of the carbon host. The benefits of such

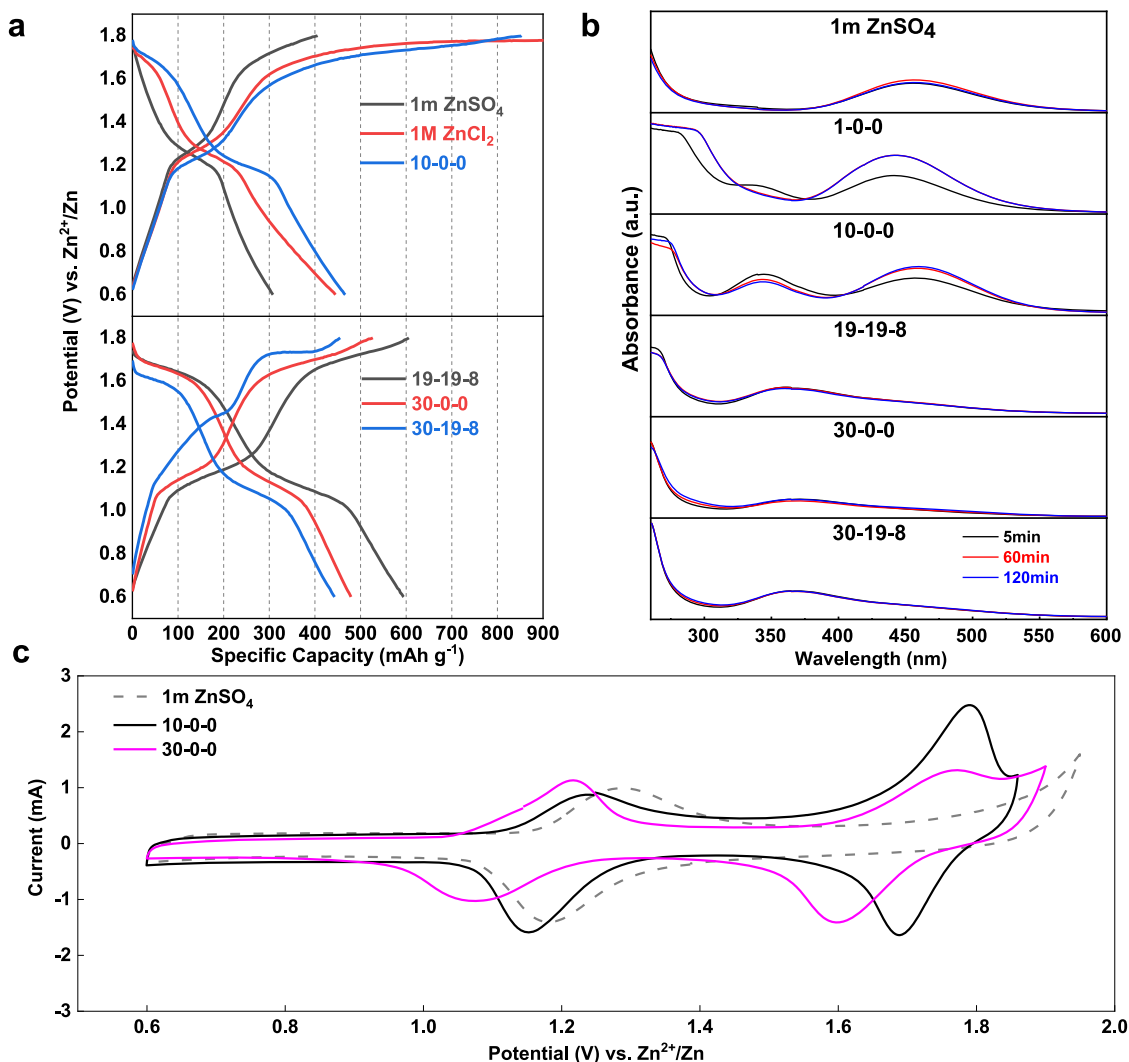
new iodine chemistry are twofold: (1) the four-electron conversion doubles the capacity been achieved in previous studies involving iodine as the cathode; (2) the reversible conversion of I<sub>2</sub> ↔ I<sup>+</sup> occurs at a much higher potential compares to the I<sub>2</sub> ↔ I<sup>-</sup> conversion (1.83 vs. 1.29 V, vs. Zn/Zn<sup>2+</sup>), guaranteeing a higher energy density. The energy density of the proposed battery is as high as 750 Wh kg<sup>-1</sup> based on the iodine mass (495 Wh kg<sup>-1</sup> based on the total active mass of cathode and anode), which is of great advantage among other sorts of energy system reported before. More importantly, an ultra-long cycle performance of 6000 cycles is achieved, with only 0.003% capacity decay per cycle.

## Results

**Four-electron conversion of iodine in aqueous solution.** Simply charge/discharge the iodine electrode (15–20 wt% iodine loaded in PAC carbon) in 1 M ZnSO<sub>4</sub> solution between 0.6 and 1.6 V vs. Zn/Zn<sup>2+</sup> shows the typical voltage profile corresponding to the reversible conversion between I<sup>-</sup> and I<sub>2</sub>, which was well established in the aqueous Zn-I<sub>2</sub> batteries. A pronounced charge plateau at 1.7 V was arisen when the cut-off voltage was enlarged up to 1.8 V vs. Zn/Zn<sup>2+</sup> that is far below the oxygen evolution potential (Fig. 1a). This process is ascribed to further oxidation of I<sub>2</sub>, however, no high-order discharge plateau was detected for the subsequent discharge process, indicating the irreversibility of high-valence iodine in the solution, or even unstable in terms of decomposition. The latter is supported by the UV-Vis absorption spectra of the blend solution of commercial ICl and 1 M ZnSO<sub>4</sub> electrolyte (Fig. 1b), showing a rapid decay of the ICl band between 340 and 360 nm<sup>31</sup>. Meanwhile, the I<sub>2</sub> peak around 460 nm became dominant. Accordingly, a dark precipitate was detected at the bottom of the solution (Supplementary Fig. 1), indicating the transformation from unstable I<sup>+</sup> to I<sub>2</sub> (Note 1 in Supplementary Information). The most straightforward approach to achieve the reversible conversion of the I<sup>+</sup>/I<sub>2</sub> couple is thus relying on tuning the activity of H<sub>2</sub>O in the electrolyte solution to suspend the hydrolysis.

Early works conducted by Kolthoff and Jordan have systematically studied the I<sup>-</sup>/I<sub>2</sub> redox processes<sup>32,33</sup>, indicating that under specified conditions both iodide and iodine yield an anodic wave corresponding to the formation of positive iodine (I<sup>+</sup>). Further studies<sup>34,35</sup> concluded that IO<sub>3</sub><sup>-</sup> was the direct oxidation product of iodine in the absence of halide (Cl<sup>-</sup>, Br<sup>-</sup>) or cyanide (CN<sup>-</sup>) in an aqueous solution. This is due to the interaction between electrophilic I<sup>+</sup> and nucleophilic species like halide<sup>36</sup>, cyanide<sup>32</sup>, and amines<sup>37</sup> which afford to charge-transfer complexes<sup>38</sup>.

ZnCl<sub>2</sub> was chosen to coordinate with H<sub>2</sub>O molecule so as to suppress the I<sup>+</sup> cation hydrolysis due to three reasons: (1) high solubility in water (up to 31 M, molality); (2) the redox potential of Cl<sub>2</sub>/Cl<sup>-</sup> is high enough (1.396 V vs. SHE) to tolerate I<sup>-</sup>/I<sub>2</sub>/I<sup>+</sup> conversion than that of Br<sub>2</sub>/Br<sup>-</sup> (1.087 V)<sup>33</sup>; (3) the nucleophilic ability of Cl<sup>-</sup> is relatively strong enough to form stable but of redox activity ICl compared with less stable IBr or non-electrochemical ICN. LiCl was introduced into ZnCl<sub>2</sub> solution to provide extra Cl<sup>-</sup> source to the parental solution. It possesses high solubility and miscibility with ZnCl<sub>2</sub> compared with its analogous alkali halides, along with the specific solvation nature of lithium cation, could further regulate the coordination between Zn<sup>2+</sup>, H<sub>2</sub>O, and Cl<sup>-</sup>. Acetonitrile (ACN), one of the most oxidative resistance solvents (above 4.8 V vs. Li<sup>+</sup>/Li), is acted as a diluent to facilitate ion mobility. Moreover, ACN is inert to I<sup>+</sup> which is obviously of great advantage in our system. The electrolyte formula we defined is the blends of specific molality of ZnCl<sub>2</sub>, LiCl, and ACN in water (donated as x-y-z). Extensive ion coordination in the concentrated electrolyte pushes the



**Fig. 1** Electrochemical behaviors and UV spectrum characterizations of zinc-iodine battery with different electrolytes. **a**, **b** Charge and discharge voltage profiles of various electrolytes at  $400 \text{ mA g}^{-1}$  along with UV-vis spectrum of ICl in these solutions recorded with time. **c** Cyclic voltammetry (CV) profiles of selected electrolytes with/without  $\text{Cl}^-$  at  $0.5 \text{ mV s}^{-1}$ .

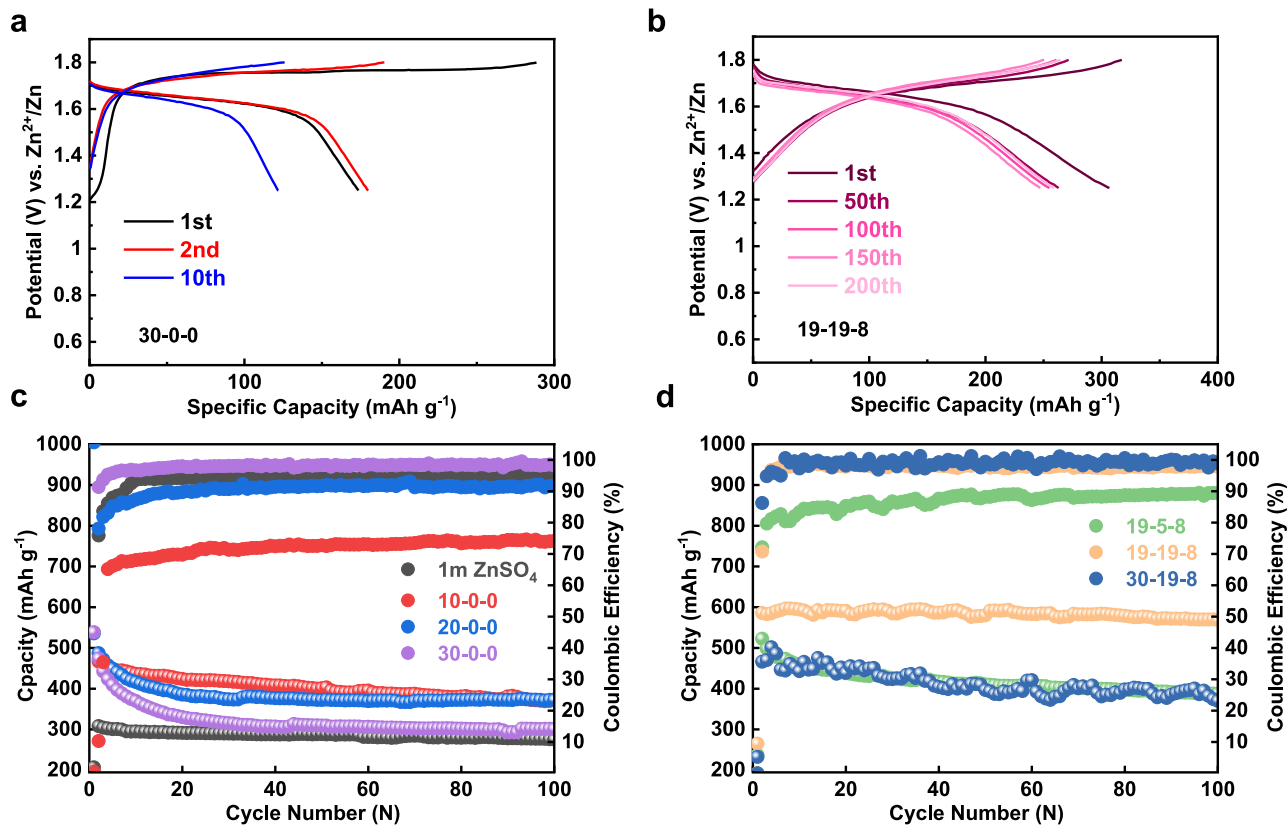
electrochemical window of the aqueous electrolyte to higher potentials (Supplementary Fig. 2).

The UV-Vis absorption spectra of the less concentrated electrolytes (1-0-0, 10-0-0) resemble the tendency of  $\text{I}^+$  decomposition in the  $1 \text{ m ZnSO}_4$  solution (Fig. 1b). In contrast, enhanced capability to stabilize ICl could be achieved in concentrated systems (19-19-8, 30-19-8, 30-0-0). Little intensity changes of the ICl band was observed in the whole duration without the appearance of the  $\text{I}_2$  signal.

The correlation of the electrolyte formula and the iodine redox chemistry were conveyed by galvanostatic charge/discharge (GCD). Distinctive discharge plateaus at  $1.75 \text{ V}$  (absent in the  $1 \text{ m ZnSO}_4$  electrolyte) are observed in the chloride-containing electrolyte even in the diluted  $1 \text{ m ZnCl}_2$  solution (Fig. 1a). Though it was still plugged by  $\text{I}^+$  ion hydrolysis as reflected by the low reversibility, we ascribe it to the nucleophilic  $\text{Cl}^-$  which provides affinity to the  $\text{I}^+$  ions. It is obvious that the high-order discharge plateau became pronounced with the increase of the  $\text{ZnCl}_2$  concentration, indicating suppressed  $\text{I}^+$  ion hydrolysis. The  $30 \text{ m ZnCl}_2$  electrolyte delivers a specific capacity of  $550 \text{ mAh g}^{-1}$  and the 19-19-8 hybrid electrolyte reveals a striking reversible capacity as high as  $594 \text{ mAh g}^{-1}$  at  $400 \text{ mA g}^{-1}$  (Fig. 1a). Note that these capacities are beyond the theoretical capacity of

$422 \text{ mAh g}^{-1}$  based on the  $\text{I}^+ \leftrightarrow \text{I}_2 \leftrightarrow \text{I}^-$  conversion. We ascribe it to the capacitance behavior of the active carbon host<sup>39,40</sup>, which shows a specific capacity of  $\sim 38 \text{ mAh g}^{-1}$  based on the carbon weight (or  $\sim 180 \text{ mAh g}^{-1}$  based on the iodine mass) with typical capacitance response in the electrolytes (Supplementary Fig. 3). This is in accordance with the contribution of porous carbons in the conventional Zn- $\text{I}_2$  batteries<sup>41</sup>. The CV curves in these electrolytes are shown in Fig. 1c and Supplementary Fig. 4. The  $1 \text{ m ZnSO}_4$  electrolyte presents only one reversible redox peak in the absence of  $\text{Cl}^-$ , showing the  $\text{I}^-/\text{I}_2$  conversion around  $1.28 \text{ V}/1.19 \text{ V}$ . However, the introduction of  $\text{Cl}^-$  introduces an additional redox couple appearing at  $1.75/1.65 \text{ V}$ . Such new couple is in accordance with previous reports<sup>33</sup>, which is attributed to the redox of  $\text{I}_2/\text{I}^+$ .

Comparison is made between the single salt electrolyte (30-0-0) and the hybrid electrolyte (19-19-8), showing that the hybrid electrolyte delivers a higher discharge capacity with nearly equal contribution from the high-order and the low-order plateau (Fig. 1a). It is apparent that the total specific capacity of the iodine electrode between  $0.6$  and  $1.8 \text{ V}$  ( $\text{I}^+ \leftrightarrow \text{I}^-$ ) is determined by  $\text{I}^+ \leftrightarrow \text{I}_2$  conversion, which is governed by the tendency of  $\text{I}^+$  ion hydrolysis. We tested the iodine electrode between  $1.25$  and  $1.8 \text{ V}$  with only the  $\text{I}_2/\text{I}^+$  conversion being activated (Fig. 2a, b). The



**Fig. 2** Electrochemical performances iodine electrode in various electrolytes. **a, b** Charge and discharge voltage profiles of the 30-0-0 and 19-19-8 electrolyte from 1.25 to 1.8 V at  $400 \text{ mA g}^{-1}$ , respectively. **c, d** Full-range (0.6–1.8 V) cycling performance of different systems at  $400 \text{ mA g}^{-1}$ .

hybrid 19-19-8 electrolyte possesses more stable capacity retention than 30-0-0 and other dilute electrolytes. The cycle performance of pure  $\text{ZnCl}_2$  solution with different molality has been revisited as well (Fig. 2c). While the coulombic efficiency is in direct proportion to concentration, the 30 m  $\text{ZnCl}_2$  system showing minimal hydrolysis of  $\text{I}^+$  is still suffered severe capacity decay. We attribute this unsatisfactory performance to the formation of non-electroactive Zn-I clusters during cycling (Supplementary Fig. 5), which is in accordance with the phenomenon reported by Ji et al.<sup>42</sup>

Apart from an abnormal potential curve with a significant voltage gap between charge/discharge plateau in 30-19-8 electrolyte, the distinct fluctuation of Capacity-CE profile is attributed to its high viscosity (Figs. 1c, 2d). On the other hand, the 19-5-8 system only exhibits a low coulombic efficiency, which is analogous to the 20 m pure  $\text{ZnCl}_2$  due to a conspicuous degree of hydrolysis (Fig. 2c, d). We further quantified the self-discharge by testing the retained capacity after storage of a charged  $\text{Zn-I}_2$  cell at open-circuit voltage (OCV) (Supplementary Fig. 6). There was significant capacity decay with progressive OCV fading for the 19-5-8 cell, whereas both 30-19-8 and 19-19-8 cells preserve high capacity and high OCV after the storage. Supplementary Fig. 6e confirms that the capacity loss during the intervals (self-discharge) in the 19-19-8 electrolyte could be recovered in the following cycles. These electrochemical results are in good agreement with the UV-vis spectrum discussed in Fig. 1. We note the proposed four-electron transfer  $\text{Zn-I}_2$  battery could also be started from the discharged state with dissolved  $\text{ZnI}_2$  in the electrolyte, as demonstrated by 0.1 M in the 30-0-0 electrolyte (Supplementary Fig. 7). Only a blank carbon electrode was used as the cathode in this case. The lower coulombic efficiency of the  $\text{Zn-ZnI}_2$  battery than that of the  $\text{Zn-I}_2$  battery emphasizes the

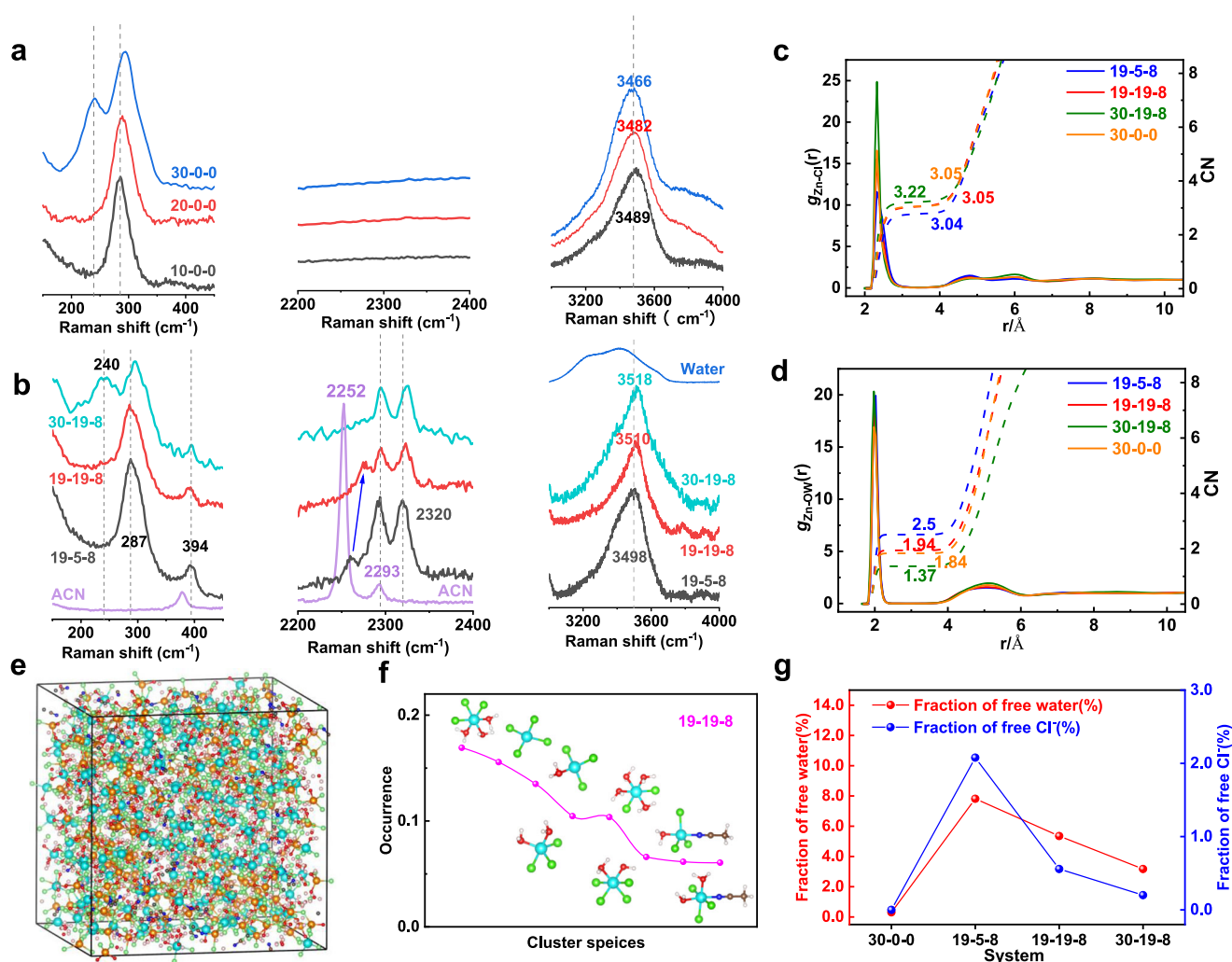
importance of physical confinement of the preloaded iodine by PAC hosts.

It is apparent that a suitable concentration is required to allow the normal operation of the battery to suppress the self-discharge reaction. We speculate the enhanced stability towards  $\text{I}^+$  species is correlated to the suppressed water activity and the sufficient chloride ions in the concentrated solution, which will be further discussed in the next section.

#### Understanding the chemistry of the four-electron conversion.

Raman spectroscopy combined with molecular dynamics simulations (MD) were conducted to get insight into the solution structure and solvation environment of the electrolytes, for the purpose of illustrating the deep distinctions of their electrochemical performance. The main response region of the Zn-Cl vibration located from 150 to  $450 \text{ cm}^{-1}$  is shown in Fig. 3a, b. The intense Raman band at around  $290 \text{ cm}^{-1}$  represents the signal of the Cl associated Zn hydrates  $[\text{ZnCl}_{2+x}(\text{H}_2\text{O})_y]^{x-}$ , existing in all solutions surveyed<sup>43,44</sup>. With increasing the content of chloride salt, another peak at  $240 \text{ cm}^{-1}$  emerged which is attributed to the tetra-coordinated  $\text{ZnCl}_4^{2-}$  cluster in 30-0-0 and 30-19-8 solution, suggesting a large portion of  $\text{Zn}^{2+}$  ions were surrounded tightly by  $\text{Cl}^-$  due to insufficient water molecules around the cations that forming the hydration shells. The  $\text{ZnCl}_4^{2-}$  clusters are absent in other solutions with less salt concentrations.

The ACN solvent has two peaks appearing at 2252 and  $2293 \text{ cm}^{-1}$  which is assigned to  $\nu(\text{CN})$  stretching vibration and a combination band, respectively<sup>45</sup>. New peaks are readily observed at 394 and  $2320 \text{ cm}^{-1}$  when ACN was introduced in  $\text{ZnCl}_2$  solutions, corresponding to the  $\nu(\text{CN})$  stretching mode of the ACN bound with  $\text{Zn}^{2+}/\text{Li}^+$  ions in the first coordination



**Fig. 3** MD simulation and Raman spectrum characterization on the properties of electrolytes. **a, b** Raman spectra of solutions of different concentrations. **c, d** Radial distribution function (RDF) of the solutions. The solid lines are the radial distribution functions, and dotted lines are the coordination numbers. **e** A snapshot of the MD simulation box for 19-19-8 system, along with the dominant clusters existing in such system (**f**). Clusters and their occurrence in the 19-19-8 system. Cyan-blue atom is  $\text{Zn}^{2+}$ , green atom is  $\text{Cl}^-$ , yellow atom is  $\text{Li}^+$ , red atom is O, dark blue atom is N, brown atom is C, gray atom is Me, and white atom is H. **g** Summary of free water and  $\text{Cl}^-$  content extracted from the MD simulation.

sphere<sup>46,47</sup>. In the meanwhile, the peak of free ACN shows a blue-shift to  $2263\text{ cm}^{-1}$  in 19-5-8 and further shifts to  $2276\text{ cm}^{-1}$  in 19-19-8. Such phenomenon is attributed to the interaction between ACN and the coordinated water molecules—the enlarged content of those water molecules solvating with cation ion results in a shift of the ACN to a higher frequency<sup>47,48</sup>. These phenomena are in accordance with the characteristic C-C  $\nu_4$  band of ACN ( $918\text{ cm}^{-1}$ , Supplementary Fig. 8). A much distinguished blue-shift observed in 19-19-8 compared with 19-5-8 further renders a higher ratio of coordinated water in the solution. The  $\nu(\text{CN})$  stretching vibration faded away successively, and finally vanished in 30-19-8 solution<sup>45</sup>. We summarized the free ACN fraction in these bi-salt electrolytes by MD simulation (Supplementary Fig. 9), based on the coordination numbers at the first solvation shell of the  $\text{Zn}^{2+}$  and  $\text{Li}^+$  ions (Supplementary Fig. 10). The limited occurrence number of acetonitrile around cations is mostly because of its preferential solvation by water and anions. The high ratio free ACN molecules is in accordance with our original concept, which was designed to decrease the viscosity and to promote ion conduction.

MD simulations afford more detailed structural information of the electrolytes (19-5-8, 19-19-8, 30-19-8, and 30-0-0, see the

method in supporting information). Information about the structural properties of the environment around an ion (cation or anion) is determined from the radial distribution functions (RDF,  $g_{\alpha\beta}(r)$ ) and the corresponding average coordination numbers in the first coordination sphere. The significance of Zn-Cl and Zn-O RDF, determined by the magnitude of peaks, indicating strong ion association and ion hydration mostly took place around the  $\text{Zn}^{2+}$  ions (Fig. 3c, d). Other cases of coordination are shown and discussed in Supplementary Fig. 10 for clarity. The Zn-Cl association is enhanced with the increase of the salt concentration, whereas the hydration is weakened at a high concentration. This, combined with the varies of the coordination number in the nearest shell, indicating a possible transformation of hydrated  $\text{Zn}^{2+}$  ion to Zn-Cl association at high concentrations. The transformation is attributed to the higher chloride ion population in the solution at high salt concentrations, which is demonstrated by the occurrence of the overall average coordination numbers, and the respective Zn- $x\text{Cl}$  and Zn- $y\text{H}_2\text{O}$  coordination analysis (Supplementary Fig. 11). Indeed, the salt concentration has a significant impact on the cluster structure and its occurrence in the electrolyte, as shown by the simulation boxes and the corresponding distribution occurrence

of the clusters (Fig. 3e, f, and Supplementary Fig. 12). High-concentration chloride ions repel H<sub>2</sub>O molecules from the hydration shell, resulting in clusters with less hydrated structure, namely, the most dominant [ZnCl<sub>3</sub>(H<sub>2</sub>O)<sub>3</sub>]<sup>-</sup> clusters in 19-19-8 solution vs. [ZnCl<sub>3</sub>(H<sub>2</sub>O)]<sup>-</sup> or even clusters without hydration [ZnCl<sub>4</sub>]<sup>2-</sup> in 30-0-0 and 30-19-8 solutions. This is consistent with the RDF analysis and their corresponding coordination number, and also obeys to the Raman results. However, the lower occurrence of hydrated cluster structure does not imply a high fraction of free H<sub>2</sub>O in solutions with high salt ratios, as shown Fig. 3g. Adversely, the free water decreases with the increase of the salt concentration. It is attributed to more cations presented in the concentrated solution that widely harvest the water molecules, which is also reflected by the overall Zn-γH<sub>2</sub>O coordination analysis (Supplementary Fig. 11). The free chloride ion in different solution has a similar tendency as the free H<sub>2</sub>O, with the 19-5-8 solution has the highest free Cl<sup>-</sup> ions ratio (2%). This is owing to the globally formation of Zn-Cl...Zn-Cl and Li-Cl...Li-Cl polymeric chain in high-concentration solutions (Fig. 3e, and Supplementary Fig. 12), which suppresses the chloride ion exchange between the bulk solution and coordinated clusters. Notably, the 19-19-8 solution has moderate fraction of free chloride ion (0.6%) and free H<sub>2</sub>O (5%) simultaneously.

Supplementary Fig. 13 shows the physicochemical properties of viscosity and ionic conductivity. In pure ZnCl<sub>2</sub> solutions, 30-0-0 owns the highest viscosity (397 cp) and lowest ionic conductivity (8.14 mS/cm). The tightly coordinated ZnCl<sub>4</sub><sup>2-</sup> cluster ascribes the large viscosity and the low ionic conductivity of the concentrated solution. Taking water in bisalt system into consideration, similar properties can be observed in 30-19-8 (339 cp and 14.5 mS/cm, respectively). However, the ionic conductivity of 19-19-8 does not bear any compromise compared with 19-5-8, even in the same level of 20-0-0, which is benefited from its relatively low viscosity (75.8 cp). The ionic conductivity of the 19-19-8 electrolyte is five times lower than that of the 1 M ZnSO<sub>4</sub> electrolyte (28 vs. 145 mS/cm), but it is sufficient for battery application.

We conclude that in dilute ZnCl<sub>2</sub> solutions (10-0-0, 20-0-0, and 19-5-8), high water activity rendering rapid hydrolysis of ICl, which results in low coulombic efficiency as discussed in Fig. 2. Whereas in solutions with very high concentrations (30-0-0 and 30-19-8), the low Cl<sup>-</sup> activity and the substantial coordination of iodide with Zn<sup>2+</sup> (Zn-I clusters, Supplementary Fig. 5) is attributed to the rapid capacity decay. Only the 19-19-8 solution takes full advantages of low fraction of free water to suppress I<sup>+</sup> hydrolysis and sufficient ionic conductivity with high Cl<sup>-</sup> activity to realize good performance.

To illustrate the involved four-electron reaction mechanism, ex situ UV-vis spectrum associated with in situ Raman spectroscopy were conducted to verify the electrode species and its stability during charge/discharge (Fig. 4). Figure 4a, b convey the ex situ UV-vis spectrum in the course of charge/discharge process in 19-19-8 electrolyte. An adsorption peak arising at 460 nm was attributed to the formation of iodine molecules when charge to 1.2 V, which confirms the conversion of iodide to iodine for the first charge plateau. It is noteworthy that, in contrast to the conventional organic metal-iodine battery, no peak of triiodide I<sub>3</sub><sup>-</sup> was detected in the whole duration (see inserted spectrum)<sup>41</sup>, suggesting a direct conversion of -1 and 0 valence iodine species. Further charge of the electrode generates another adsorption peak at around 342 nm, in analogous to the previous reports<sup>49</sup>, which is assigned to the formation of ICl interhalogens.

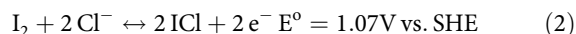
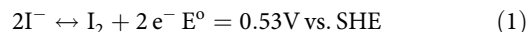
We evaluated the interaction of iodide (discharge state) with the electrolyte by MD simulations. The significance of Zn-I coordination of the 30-0-0 solution is much stronger than

the 19-19-8 system, as determined by the magnitude of the first coordination shell (RDF results, Supplementary Fig. 14). This indicates iodide ion could participate in cation coordination in 30-0-0 system (contact ion pair, CIP), which might drag the iodide diffuse from the electrode. However, the iodide and zinc coordinated as a solvent-separated ion pair (SSIP, indirect interaction) in the 19-19-8 solution. The CIP coordination of zinc-iodide might attribute to the formation of the non-electroactive ZnI<sub>2</sub>(OH<sub>2</sub>)<sub>2</sub> clusters in the 30-0-0 electrolyte (Supplementary Fig. 5), which leads to capacity fading in the battery.

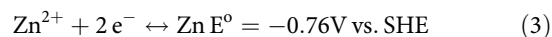
Real-time transformation of the iodine species was monitored by in situ Raman spectroscopy within a Raman electrolytic device (Supplementary Fig. 15, Fig. 4c). The major peak detected at 288 cm<sup>-1</sup> among the whole course is assigned to [ZnCl<sub>2+x</sub>(H<sub>2</sub>O)<sub>y</sub>]<sup>2-x</sup> clusters<sup>45</sup>, which again demonstrates the main coordination state of the electrolyte solution. The new Raman signal emerged around 202 cm<sup>-1</sup> when charge to 1.4 V is corresponding to the characteristic band of ICl species<sup>50,51</sup>. The iodine intermediate was proved to form during the first charge plateau by the ex situ UV-vis spectrum. However, its Raman signal is failure to be detected under such experimental parameters, even absent in 1 m ZnSO<sub>4</sub> solution (Supplementary Fig. 15), which is in consistent with previous reports<sup>41</sup>. During discharge, the ICl peak faded away with the discharge depth and vanished eventually at the end of high-order plateau, again indicating a reversible I<sup>+</sup>/I<sub>2</sub> conversion. In situ Raman characterization of other systems (1 m ZnSO<sub>4</sub> and 30 m ZnCl<sub>2</sub>, Supplementary Fig. 16) show identical iodine speciation in the 30 m ZnCl<sub>2</sub> solution but only I<sub>2</sub>/I<sup>-</sup> conversion occurred in 1 m ZnSO<sub>4</sub> solution. Note that none Raman signal of Zn(I<sub>3</sub>)<sub>2</sub> was found neither in concentrated electrolytes (30 m ZnCl<sub>2</sub>) nor in 1 m ZnSO<sub>4</sub> system.

Based on the electrochemical analysis and spectral results, we depict a clear portrait of the reaction mechanism for the four-electron conversion:

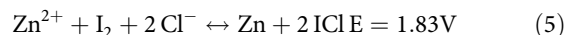
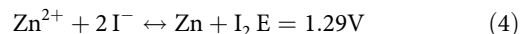
Cathode:



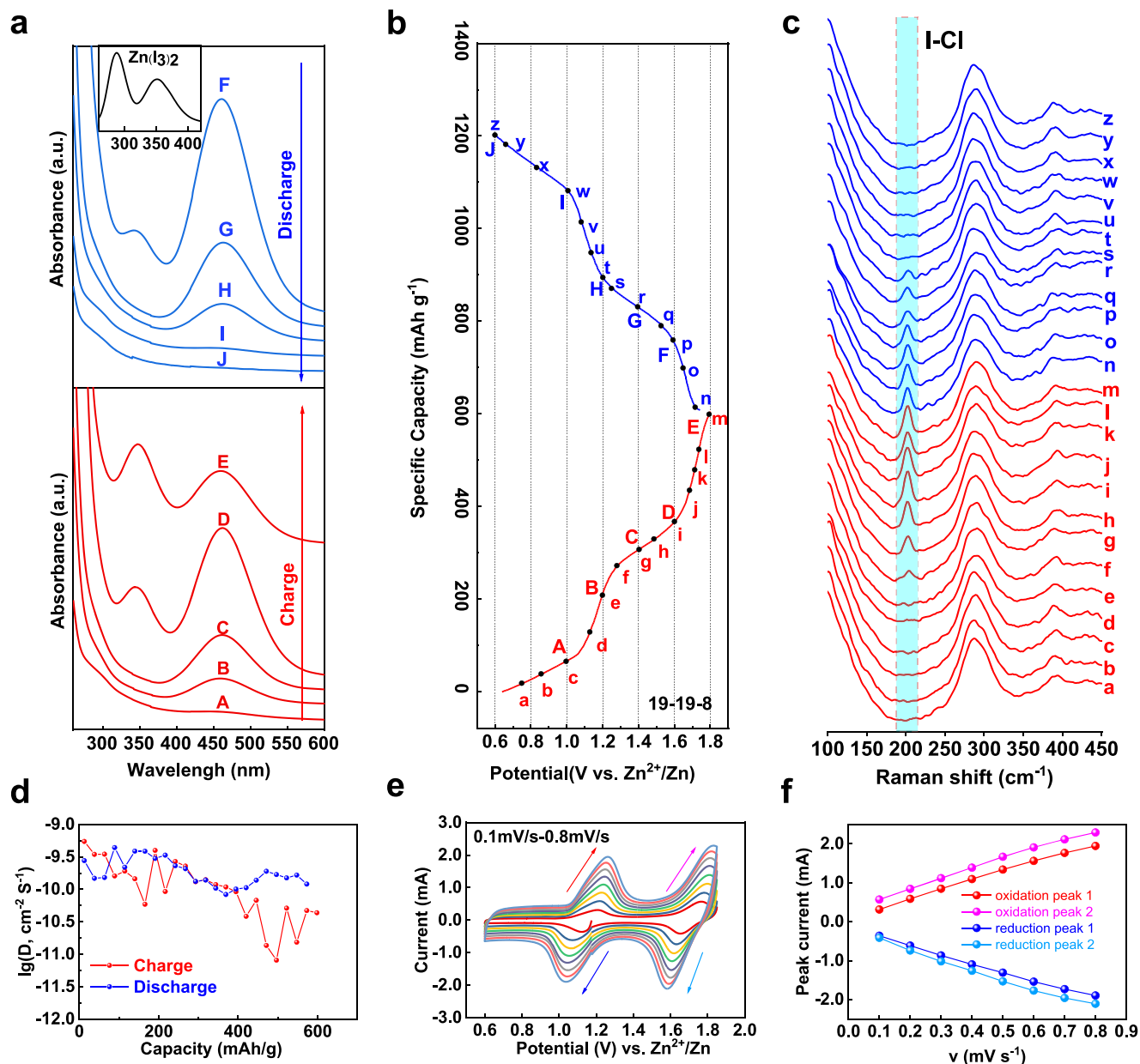
Anode:



Total reaction:



Galvanostatic intermittent titration technique (GITT) was used to study the kinetics of reactions (Supplementary Fig. 17, see method for details). The quasi-equilibrium potentials are about 1.18 V for I<sup>-</sup>/I<sub>2</sub> and about 1.71 V for I<sub>2</sub>/ICl oxidation, respectively. The diffusion coefficient yielded from GITT is in the order of 10<sup>-9</sup>–10<sup>-10</sup> cm<sup>2</sup> s<sup>-1</sup> (Fig. 4d). CV curves of the 19-19-8 system with different sweep rates from 0.1 to 0.8 mV s<sup>-1</sup> are shown in Fig. 4e. The linearly increased oxidation and reduction peak-current (*i*) as a function of the root of scan rates (*v*<sup>1/2</sup>), indicates both I<sup>-</sup>/I<sub>2</sub> and I<sub>2</sub>/I<sup>+</sup> conversions are diffusion-controlled redox reactions (Fig. 4f). Moreover, kinetic analyzing adopts from the log *i*–log *v* plots (Supplementary Fig. 18) show the slope of the peaks at lower potential is normally higher than that at the higher potential (either reduction or oxidation), indicating the conversion of I<sup>-</sup>/I<sub>2</sub> is faster than the I<sub>2</sub>/I<sup>+</sup> redox couple.

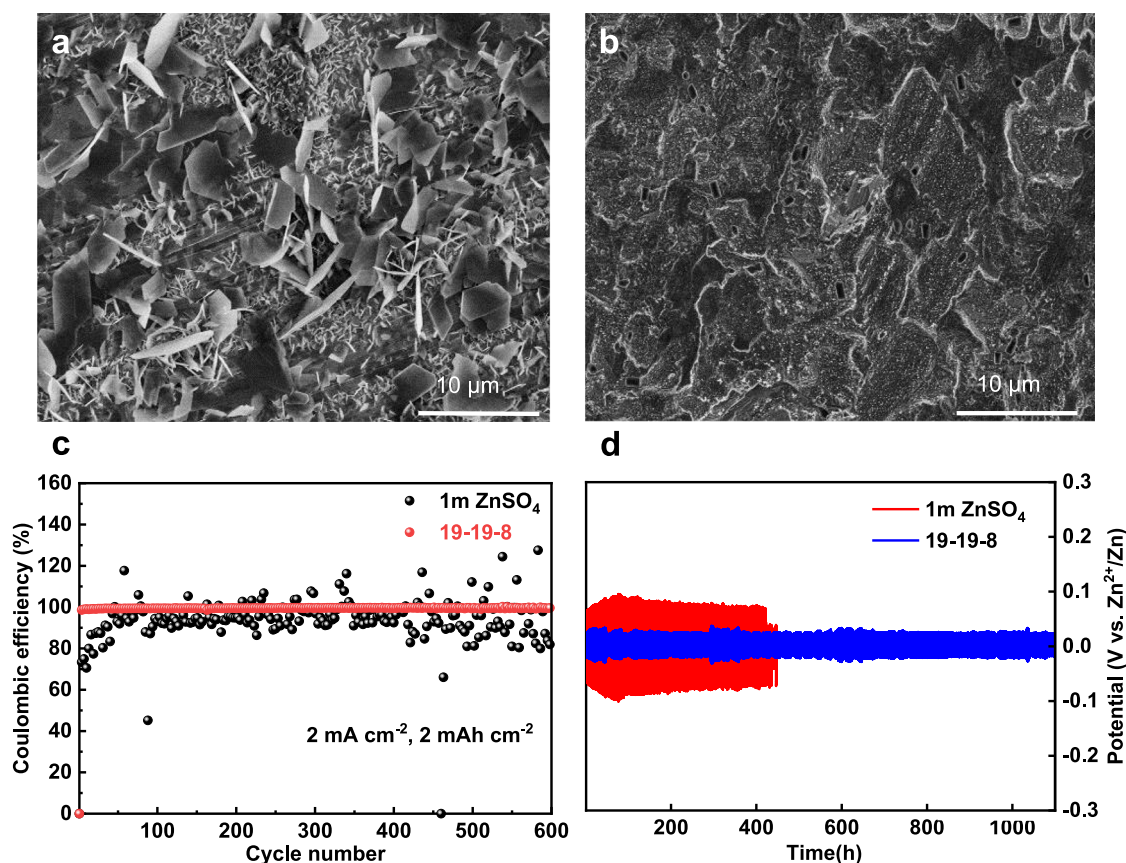


**Fig. 4** Spectrum and electrochemistry characterizations to reveal the mechanism of the four-electron conversion process. **a** Ex situ UV vis spectrum of 19-19-8 system recorded at different charge-discharge stages. **b** Typical voltage-capacity profile of 19-19-8. **c** In situ Raman spectrum of 19-19-8 system during charge/discharge. **d** Diffusion coefficient versus specific capacity, calculated from GITT measurements. **e** CV curves with different scanning rates from 0.1 to 0.8 mV s<sup>-1</sup>. **f** The plots of the oxidation and reduction peak-current with the function of the root of scanning rates.

**A high energy density aqueous Zn-I<sub>2</sub> battery based on four-electron conversion.** The electrolyte formula (19-19-8) we proposed has the advantage of suppressed H<sub>2</sub>O activity and preserved free chloride ions, which facilitate the four-electron conversion of iodine with a high reversible capacity. While a practical battery relies on the robust anode as well, we tested the zinc anode in the 19-19-8 electrolyte to elucidate the electroplating behavior.

It is apparent that zinc anode suffers serious dendrite formation in normal aqueous solution (1 M ZnSO<sub>4</sub>), as shown in Fig. 5a. The plated zinc anode shows two series of morphologies, namely polygons plates and clusters both with sharp edges. The disadvantages of these dendrites are twofold: they might pierce through the separator leading to a short-circuit and the high surface area dendrite could result in detrimental side

reaction with electrolyte. The latter is illustrated by the deteriorative coulombic efficiency of the Zn||Ti battery in the 1 M ZnSO<sub>4</sub> electrolyte (Fig. 5c). In sharp contrast, the zinc plated in the 19-19-8 electrolyte shows dense and smooth morphology with the same test condition (Fig. 5b). The morphology of the zinc anode after long-term cycling further confirms the favorable electrodeposition in the 19-19-8 electrolyte (Supplementary Fig. 19). The less dendritic deposition is attributed to the aggregated ion density at high ZnCl<sub>2</sub> concentration suppressing the ion-depletion, which is regarded as the main reason for dendrite nucleation<sup>43</sup>. Plating/stripping in Zn||Zn symmetric cells (1 mA cm<sup>-2</sup>, 1 h) further demonstrates the robust of the zinc anode in the 19-19-8 electrolyte (Fig. 5d). The 19-19-8 electrolyte sustains highly stable voltage profile over 1100 hours without any significant overpotential fluctuation, whereas the 1 M ZnSO<sub>4</sub>



**Fig. 5** Characterization of the Zn metal anode in the electrolyte. **a, b** SEM images of the Zn electrodes cycled for 1 h at 1 mA cm<sup>-2</sup> in 1 m ZnSO<sub>4</sub> and 19-19-8, respectively. **c** Coulombic efficiencies of zinc plating/stripping on Ti foil (2 mA cm<sup>-2</sup>, 1 h for the plating). **d** The plating/stripping in Zn||Zn symmetric cells at 1 mA cm<sup>-2</sup> with a sweep duration of 10 min.

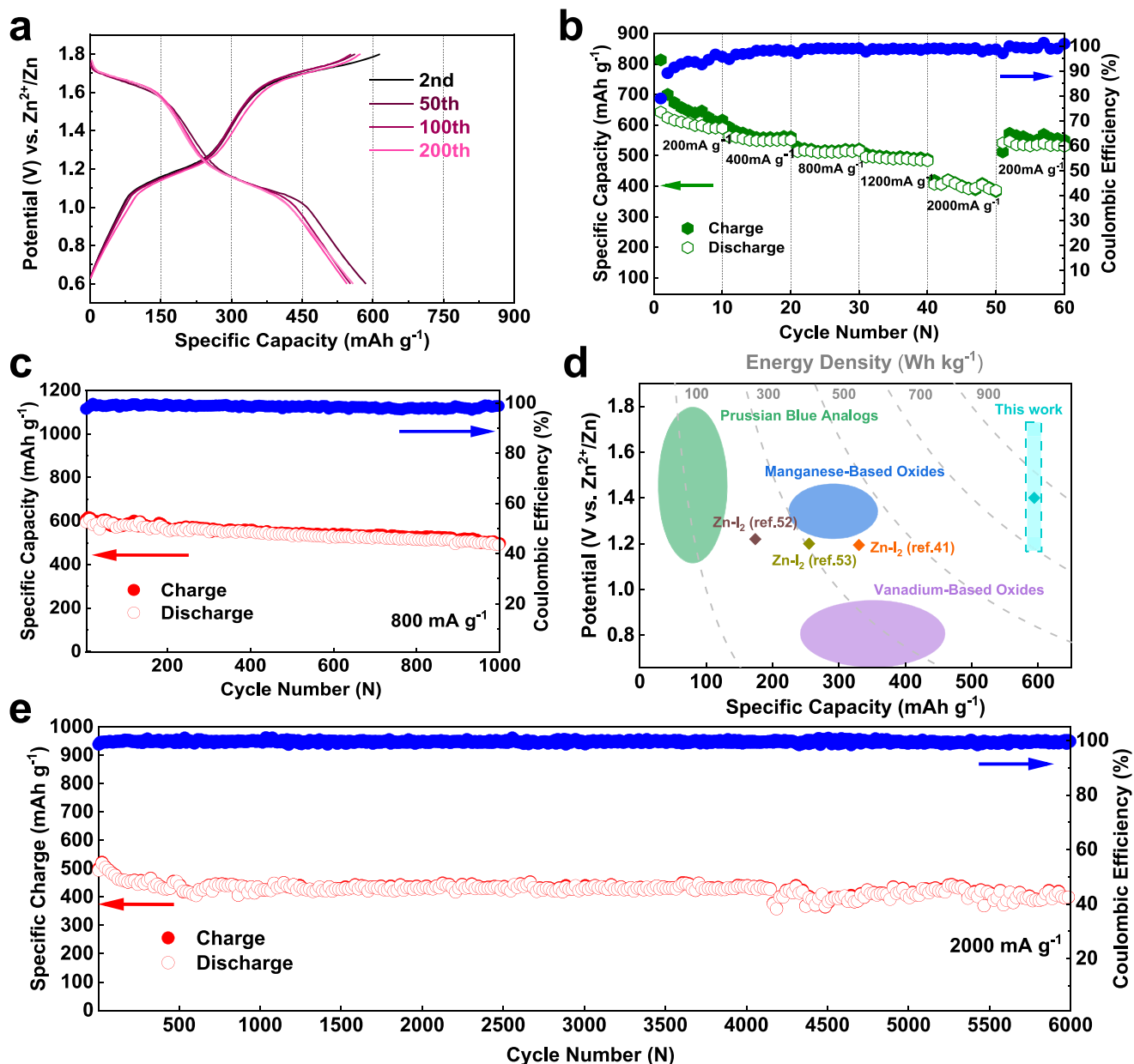
electrolyte shows higher overpotential and the cell is only stable for about 400 h. Moreover, the Zn||Ti battery in the 19-19-8 electrolyte shows a coulombic efficiency of 99.8% for over 600 cycles (Fig. 5c). The highly reversibility of the zinc anode in the 19-19-8 electrolyte is benefited from the suppressed H<sub>2</sub>O activity that mitigates the formation of Zn(OH)<sub>2</sub>/ZnO<sup>43</sup>.

The cycling performance of the zinc iodine battery was performed with iodine loaded active carbon electrode. Iodine was loaded onto active carbons by physical adsorption in water, as confirmed by the mass changes and the surface area variations of the composite (Supplementary Fig. 20). EDS mapping reveals that iodine is homogeneously distributed on the electrode (Supplementary Fig. 21). XPS characterization of the sample shows a splitting of the core-level spectra of I<sub>3d</sub>, indicating electron transformation between iodine and the carbon matrix (Supplementary Fig. 22)<sup>52</sup>. Given the fact the Zn-I<sub>2</sub> battery was assembled at the middle valance state of iodine, we confirmed that there is little difference for the cell that being activated by charge or by discharge (Supplementary Fig. 23). Supplementary Fig. 24 shows the cycling performance of the Zn-I<sub>2</sub> battery in a flooded electrolyte condition (80, 160 μL), demonstrating similar performance as the 50 μL cells. A slight capacity fading is observed from the charge/discharge curves at a low current density of 400 mA g<sup>-1</sup> for over 200 cycles; and a coulombic efficiency of 98.5% was obtained (Fig. 6a). Rate capability was examined from 200, 400, 800, 1200 to 2000 mA g<sup>-1</sup>, showing high reversible capacities of 609, 589, 530, 507, 419 mAh g<sup>-1</sup>, respectively (Fig. 6b). The coulombic efficiencies at these rates are very high, rendering controlled I<sup>+</sup> hydrolysis (self-discharge).

Long cycling performance at a moderate rate of 800 mA g<sup>-1</sup> (around 90 min per cycle) indicated a very promising capacity retention at 85.4% after 1000 cycles (Fig. 6c). The reliability of four-electron conversion was also examined at a remarkable high current density of 2000 mA g<sup>-1</sup>, revealing a reversible capacity of 420 mAh g<sup>-1</sup> with a superior longevity as long as 6000 cycles, corresponding to a capacity decay rate of 0.003% per cycle (Fig. 6e). The remarkable long lifespan is attributed to the highly reversible I<sup>-</sup>/I<sub>2</sub> and I<sub>2</sub>/I<sup>+</sup> redox couples, while the suppressed solubility of the iodine species by the concentrated electrolyte and the physical confinement provided by the PAC carbon further ensure high utilization of iodine<sup>52</sup>. Aside from that, the stable plating/stripping of Zn anode also benefit to such notable battery performance.

Note that the formation of ICl inter-halogens was not necessarily limited by the content of free Cl<sup>-</sup> ions in the electrolyte. This was supported by the formation of ICl in the 30-0-0 electrolyte (Supplementary Fig. 16), which shows none free Cl<sup>-</sup> ions according to the MD simulation. We developed doped carbon to substitute the PAC carbon as the iodine host. Due to the porous structure and the affinity towards iodine species by the heteroatoms, high iodine loading (~45 wt% in the composite, and 9 mg cm<sup>-2</sup> in the electrode) could be achieved. This electrode has similar cycling performance as the I<sub>2</sub>/PAC electrode with the identical condition (Supplementary Fig. 25), again indicating that the four-electron redox chemistry is not simply limited by the free fraction of Cl<sup>-</sup> ion in the electrolyte. However, too high iodine mass in the cell might result in the conjugation of the electrolyte quantity and the iodine mass. This is due to the significant electrolyte diluting caused by ion





**Fig. 6** The electrochemical performance of 19-19-8. **a** Comparative voltage profiles at 400 mA g<sup>-1</sup> for 200 cycles. **b** Rate test at different current densities. **c** Cycling performance at 800 mA g<sup>-1</sup> for 1000 cycles. **d** The energy density, average voltage, and specific capacity of aqueous zinc batteries based on intercalation chemistry and conversion chemistry. For comparison, energy densities were converted with active materials only. The intercalation Zn-ion batteries were quoted from ref. <sup>12</sup>. **e** Long-term cycling at a high rate of 2000 mA g<sup>-1</sup> for over 6000 cycles.

depletion during the charge process at high iodine loading, which releases of free water to a large extent (triggers ICl hydrolysis) thus limit the reversibility.

For comparison, we plotted our four-electron conversion Zn-I<sub>2</sub> battery in Fig. 6d against other aqueous systems. The high discharge plateau of the I<sub>2</sub>/I<sup>+</sup> redox couple increases the average operational voltage of the Zn-I<sub>2</sub> battery (1.45 V vs. 1.2 V of the conventional Zn-I<sub>2</sub> batteries), affording to a high energy density of 750 Wh kg<sup>-1</sup> (base on the iodine mass). This gives a sharp demonstration of the merits of our system over typical zinc-iodine batteries<sup>41,52,53</sup>, and holds a distinct place among intercalation electrodes for aqueous zinc-ion battery<sup>12</sup> and state-of-the-art aqueous Li/Na-ion batteries<sup>54</sup>. The full-cell energy density after considering the anode mass still reaches 495 Wh kg<sup>-1</sup>, which is at the same level of the recent reported halogen intercalated graphite Li-ion battery<sup>24</sup>. The Ragone plots derived from the rate

performance further illustrate the high energy density as well as the high power density of the four-electron conversion Zn-I<sub>2</sub> battery (Supplementary Fig. 26), indicating promising applications by considering the intrinsic safety brought by its aqueous nature. Noting high iodine loading and high iodine utilization could be achieved by developing new host materials that are highly conductive and provides affinity to the iodine species during the electrochemical process.

## Discussion

In summary, we have developed an aqueous zinc-iodine battery with four-electron transfer per iodine by activating the I<sub>2</sub>/I<sup>+</sup> couple (1.83 V vs. Zn/Zn<sup>2+</sup>) in addition to the I<sup>-</sup>/I<sub>2</sub> couple (1.29 V), which doubles the capacity of the conventional iodine batteries either in organic or in aqueous media. This is correlated to the

dynamics of water and chloride ions in the electrolyte solution, as demonstrated by both spectroscopy studies and modeling, showing the molality controlled coordination behavior fully manipulates the ICl inter-halogen formation and its hydrolysis. The extended iodine chemistry in the deliberated bisalt electrolyte (19-19-8) doubles the capacity that was achieved in conventional iodine batteries, further boosting the energy density of the developed Zn-I<sub>2</sub> batteries due to the distinctive high potential. The energy density of the proposed battery is as high as 750 Wh kg<sup>-1</sup> based on the active materials mass of cathode (iodine fraction in the cathode is 15–20 wt%). More importantly, an ultra-long cycle performance of 6000 cycles is achieved with only 0.003% capacity decay per cycle. Such rechargeable Zn-I<sub>2</sub> batteries have the potential to be cost effective and safe, and to have high power density for practical application. Further studies on other types of carbonaceous or non-carbonaceous materials with stronger interaction with iodine are highly desired to ensure a high utilization of the active material. Moreover, optimizing the amount of electrolyte and the capacity matching between the cathode and anode are crucial in realizing a high energy density of the four-electron Zn-I<sub>2</sub> practical full battery.

## Methods

**Preparation of PAC-I<sub>2</sub> cathodes.** Solution-adsorption method was used for the preparation of cathodes. In brief, 300 mg of I<sub>2</sub> were mixed with 300 mg PAC, followed by adding 20 ml deionized water. The Iodine ratio in the I<sub>2</sub>/PAC composite was about 15–20 wt%, as calculated by deducting the mass of PAC from the final weighted composite. The PAC/I<sub>2</sub>, sodium carboxymethyl cellulose (CMC) and super P were mixed in deionized water with a mass ratio of 8:1:1. Then the slurry was cast on a titanium foil followed by drying for 12 h in the air at 60 °C. The electrodes were cut into disks with a diameter of 10 mm. The average areal loading of PAC-I<sub>2</sub> composite was about 4–5 mg cm<sup>-2</sup> in the electrode.

**Materials characterization.** Raman analyses were carried out on a bench Raman dispersive microspectrometer (InVia Reflex, Renishaw) using a laser (wavelength of 532 nm) at frequencies from 100 to 4000 cm<sup>-1</sup>. Raman electrolyte device was implemented for the in situ Raman test, the cathode slurry (PAC/I<sub>2</sub> with binder) loaded at the bottom of the cell (namely, glass carbon electrode) was dried at 60 °C, which is served as the working electrode. The counter electrode is Pt wire and the reference electrode is Ag/AgCl, respectively. The cell was sealed with silica window. The galvanostatical charge/discharge was conducted on a Bio-logic electrochemical station (VSP) with a current density of 0.05 mA cm<sup>2</sup>. UV-vis spectrum characterization was carried out on a UV1902PC with a range from 200 to 600 nm. XRD measurements were carried out on a Bruker D8-Advance powder X-ray diffractometer operating at 40 kV and 30 mA, using Cu-K $\alpha$  radiation ( $\lambda = 0.15405$  nm). SEM studies were carried out on a FEI QuANTA 200 environmental SEM instrument and a JSM-6700F field-emission SEM instrument. Electrodes were gently washed with deionized water to remove the electrolyte and dried for 12 h in air at 60 °C prior to the characterizations. Brunauer-Emmett-Teller (BET) measurements were carried out on a JW-BK200C surface area analyzer operating at nitrogen atmosphere and the adsorption temperature of 77 K. Samples were dried for 12 h in air at 60 °C prior to the characterization.

**Electrochemical measurements.** Electrochemical studies were performed in PFA-based Swagelok-type cells (1/2-inch diameter). Zinc foil with 0.1-mm thickness was used as the anodes. Glass fiber was placed between the anode and cathode as the separator. The electrolyte amount for each cell was 50  $\mu$ L. The cells were then galvanostatically tested on a Land BT2001A battery test system (Wuhan, China) at room temperature. For the Zn|| Zn symmetric cells, we used a protocol of 1 hour of stripping followed by 1 h of plating with a current density of 1 mA cm<sup>-1</sup> for each cycle. Cyclic voltammetry measurements and the GITT tests were performed on a VSP-3 electrochemical workstation (Bio-Logic, France) in a three-electrode cell with the Ag/AgCl reference electrode. The scanning voltage range was set from -0.4 to 0.9 V at scan rates various from 0.1 to 0.8 mV s<sup>-1</sup>. The GITT test, consisting of a series of current pulses ( $\approx 400$  mA g<sup>-1</sup>) for 1 min followed by a 10 min relaxation process, was performed with the voltage range from 0.6 V to 1.8 V (vs Zn<sup>2+</sup>/Zn).

**Computation.** Molecular dynamics simulations of four different high-concentration mixed systems were carried out with the DL\_POLY\_4.06 software package<sup>55,56</sup> to investigate the effects of microscopic hydration characteristics on battery performance. The system mainly consists of ZnCl<sub>2</sub>, LiCl, H<sub>2</sub>O or CH<sub>3</sub>CN. The molar ratios of ZnCl<sub>2</sub>:LiCl:CH<sub>3</sub>CN are 19-5-8, 19-19-8, 30-19-8, and 30-0-0, respectively, keeping the molar concentration of water unchanged. In the entire

simulation system, the density of the box is maintained at  $\sim 1$  g/cm<sup>3</sup>. Details of the simulation boxes of the four systems are shown in Supplementary Tables 1 and 2 and Supplementary Note 2.

## Data availability

The authors declare that all the relevant data are available within the paper and its Supplementary Information file or from the corresponding author upon reasonable request.

Received: 19 May 2020; Accepted: 24 November 2020;

Published online: 08 January 2021

## References

- Liang, Y. et al. A review of rechargeable batteries for portable electronic devices. *InfoMat* **1**, 6–32 (2019).
- Li, M. et al. Design strategies for nonaqueous multivalent-ion and monovalent-ion battery anodes. *Nat. Rev. Mater.* **5**, 276–294 (2020).
- Ponrouch, A., Frontera, C., Bardé, F. & Palacin, M. R. Towards a calcium-based rechargeable battery. *Nat. Mater.* **15**, 169–172 (2016).
- Aurbach, D. et al. Prototype systems for rechargeable magnesium batteries. *Nature* **407**, 724–727 (2000).
- Kundu, D., Adams, B. D., Ort, V. D., Vajargah, S. H. & Nazar, L. F. A high-capacity and long-life aqueous rechargeable zinc battery using a metal oxide intercalation cathode. *Nat. Energy* **1**, 16119 (2016).
- Lin, M. C. et al. An ultrafast rechargeable aluminium-ion battery. *Nature* **520**, 324–328 (2015).
- Xu, C., Li, B., Du, H. & Kang, F. Energetic zinc ion chemistry: the rechargeable zinc ion battery. *Angew. Chem. Int. Ed.* **51**, 933–935 (2012).
- Manthiram, A., Fu, Y., Chung, S., Zu, C. & Su, Y. Rechargeable lithium-sulfur batteries. *Chem. Rev.* **114**, 11751–11787 (2014).
- Aurbach, D., McCloskey, B. D., Nazar, L. F. & Bruce, P. G. Advances in understanding mechanisms underpinning lithium-air batteries. *Nat. Energy* **1**, 16128 (2016).
- Pang, Q., Liang, X., Kwok, C. Y. & Nazar, L. F. Advances in lithium-sulfur batteries based on multifunctional cathodes and electrolytes. *Nat. Energy* **1**, 16132 (2016).
- Yadegari, H. & Sun, X. Recent advances on sodium-oxygen batteries: a chemical perspective. *Acc. Chem. Res.* **51**, 1532–1540 (2018).
- Fang, G., Zhou, J., Pan, A. & Liang, S. Recent advances in aqueous zinc-ion batteries. *ACS Energy Lett.* **3**, 2480–2501 (2018).
- Sun, W. et al. Zn/MnO<sub>2</sub> battery chemistry with H<sup>+</sup> and Zn<sup>2+</sup> Coinsertion. *J. Am. Chem. Soc.* **139**, 9775–9778 (2017).
- Yan, M. et al. Water-lubricated intercalation in V<sub>2</sub>O<sub>5</sub>·nH<sub>2</sub>O for high-capacity and high-rate aqueous rechargeable zinc batteries. *Adv. Mater.* **30**, 1703725 (2018).
- Li, B. et al. Ambipolar zinc-polyiodide electrolyte for a high-energy density aqueous redox flow battery. *Nat. Commun.* **6**, 6303 (2015).
- Xie, C., Liu, Y., Lu, W., Zhang, H. & Li, X. Highly stable zinc-iodine single flow batteries with super high energy density for stationary energy storage. *Energy Environ. Sci.* **12**, 1834–1839 (2019).
- Lee, J.-H. et al. High-energy efficiency membraneless flowless Zn-Br battery: utilizing the electrochemical-chemical growth of polybromides. *Adv. Mater.* **31**, 1904524 (2019).
- Zhao, Q., Lu, Y., Zhu, Z., Tao, Z. & Chen, J. Rechargeable lithium-iodine batteries with iodine/nanoporous carbon cathode. *Nano Lett.* **15**, 5982–5987 (2015).
- Gong, D. et al. An iodine quantum dots based rechargeable sodium-iodine battery. *Adv. Energy Mater.* **7**, 1601885 (2017).
- Lu, K. et al. Rechargeable potassium-ion batteries enabled by potassium-iodine conversion chemistry. *Energy Storage Mater.* **16**, 1–5 (2019).
- Bertasi, F., Seppehr, F., Pagot, G., Paddison, S. J. & Di Noto, V. Toward a magnesium-iodine battery. *Adv. Funct. Mater.* **26**, 4860–4865 (2016).
- Tian, H., Zhang, S., Meng, Z., He, W. & Han, W.-Q. Rechargeable aluminum/iodine battery redox chemistry in ionic liquid electrolyte. *ACS Energy Lett.* **2**, 1170–1176 (2017).
- Wang, F. et al. A stimulus-responsive zinc-iodine battery with smart overcharge self-protection function. *Adv. Mater.* **32**, 2000287 (2020).
- Yang, C. et al. Aqueous Li-ion battery enabled by halogen conversion-intercalation chemistry in graphite. *Nature* **569**, 245–250 (2019).
- Jones, J. L. & Arranaga, A. B. A new zinc-iodate primary battery. *J. Electrochem. Soc.* **105**, 5 (1958).
- Wang, Z., Meng, X., Chen, K. & Mitra, S. Development of high-capacity periodate battery with three-dimensional-printed casing accommodating replaceable flexible electrodes. *ACS Appl. Mater. Interfaces* **10**, 30257–30264 (2018).

27. Wang, A. & Gyenge, E. L. Borohydride electro-oxidation in a molten alkali hydroxide eutectic mixture and a novel borohydride-periodate battery. *J. Power Sources* **282**, 169–173 (2015).
28. Wang, Z., Meng, X., Chen, K. & Mitra, S. High capacity aqueous periodatebatteries featuring a nine-electron transfer process. *Energy Storage Mater.* **19**, 206–211 (2019).
29. Dey, A. N. & Holmes, R. W. U.S. Patent No. 4,060,676. Washington, DC: U.S. Patent and Trademark Office (1977).
30. Yaraliev, Y. A. Electrochemistry of iodine. *Russian Chem. Rev.* **51**, 566–581 (1982).
31. Seery, D. J. & Britton, D. The continuous absorption spectra of chlorine, bromine, bromine chloride, iodine chloride, and iodine bromide. *J. Phys. Chem.* **68**, 2263–2266 (1964).
32. Kolthoff, I. M. & Jordan, J. Amperometric titration and voltammetric determination of iodide. *Anal. Chem.* **25**, 1833–1837 (1953).
33. Anson, I. M. & Jordan, J. Voltammetry of iodine and iodide at rotated platinum wire electrodes. *J. Am. Chem. Soc.* **75**, 1571–1575 (1953).
34. Anson, F. C. & Lingane, J. J. Anodic chronopotentiometry with platinum and gold electrodes. The iodide-iodine-iodate system. *J. Am. Chem. Soc.* **79**, 1015–1020 (1957).
35. Beran, Premysl & Bruckenstein, Stanley Voltammetry of iodine(I) chloride, iodine, and iodate at rotated platinum disk and ring-disk electrodes. *Anal. Chem.* **40**, 1044–1051 (1968).
36. Philbrick, F. A. The hydrolysis of iodine monochloride. *J. Am. Chem. Soc.* **56**, 1257–1259 (1934).
37. Whitaker, R. D., Ambrose, J. R. & Hickam, C. W. Iodine monochloride and iodine trichloride complexes with heterocyclic amines. *J. Inorg. Nucl. Chem.* **17**, 254–256 (1961).
38. Fialkov, Ya. A. Interhalogen compounds as complex-formers. *Russ. Chem. Bull.* **3**, 847–855 (1954).
39. Shao, Y. et al. Design and mechanisms of asymmetric supercapacitors. *Chem. Rev.* **118**, 9233–9280 (2018).
40. Zhang, L. L. & Zhao, X. S. Carbon-based materials as supercapacitor electrodes. *Chem. Soc. Rev.* **38**, 2520–2531 (2009).
41. Li, Y., Liu, L., Li, H., Cheng, F. & Chen, J. Rechargeable aqueous zinc-iodine batteries: pore confining mechanism and flexible device application. *Chem. Commun.* **54**, 6792–6795 (2018).
42. Hong, J. J. et al. A dual plating battery with the iodine/[ZnI<sub>x</sub>(OH)<sub>2</sub>]<sub>4-x</sub> cathode. *Angew. Chem.* **131**, 16057–16062 (2019).
43. Zhang, C. et al. A ZnCl<sub>2</sub> water-in-salt electrolyte for a reversible Zn metal anode. *Chem. Commun.* **54**, 14097–14099 (2018).
44. Irish, D. E., McCarrroll, B. & Young, T. F. Raman study of zinc chloride solutions. *J. Chem. Phys.* **39**, 3436–3444 (1963).
45. Edwards, H. G. M., Hoskins, A. R., Johnson, A. F. & Lewis, I. R. Raman spectroscopic determination of the dissociation constants of an acetonitrile-zinc complex in aqueous solution and the enthalpy and entropy of complex dissociation. *J. Raman Spectrosc.* **22**, 651–656 (1991).
46. Evans, J. C. & Lo, G. Y.-S. Raman and infrared studies of acetonitrile complexed with zinc chloride. *Spectrochimica Acta* **21**, 1033–1038 (1965).
47. Sze, Y.-K. & Irish, D. E. Vibrational spectral studies of ion-ion and ion-solvent interactions. III. Zinc nitrate in water/acetonitrile mixtures. *J. Solut. Chem.* **8**, 395–409 (1979).
48. Mohr, S. C., Wilk, W. D. & Barrow, G. M. The association of water with bases and anions in an inert solvent. *J. Am. Chem. Soc.* **87**, 3048–3052 (1965).
49. Gillam, A. E. & Morton, R. A. Absorption spectra in relation to the colour of solutions of iodine monochloride. *Proc. R. Soc. A: Math. Phys. Eng. Sci.* **132**, 152–167 (1931).
50. Klaeboe, P. The Raman spectra of some iodine, bromine, and iodine monochloride charge-transfer co-complexes in solution. *J. Am. Chem. Soc.* **89**, 3667–3676 (1967).
51. Person, W. B., Anderson, G. R., Fordemwalt, J. N., Stammreich, H. & Fornieris, R. Infrared and Raman spectra, force constants, and the structures of some polyhalide ions: ICl<sub>2</sub><sup>-</sup>, ICl<sub>4</sub><sup>-</sup>, BrCl<sub>2</sub><sup>-</sup>, and Br<sub>3</sub><sup>-</sup>. *J. Chem. Phys.* **35**, 908–914 (1961).
52. Pan, H. et al. Controlling solid-liquid conversion reactions for a highly reversible aqueous zinc-iodine battery. *ACS Energy Lett.* **2**, 2674–2680 (2017).
53. Bai, C. et al. A sustainable aqueous Zn-I-2 battery. *Nano Res.* **11**, 3548–3554 (2018).
54. Liu, Z. et al. Voltage issue of aqueous rechargeable metal-ion batteries. *Chem. Soc. Rev.* **49**, 180–232 (2020).
55. Todorov, I. T., Smith, W., Trachenko, K. & Dove, M. T. DL\_POLY\_3: new dimensions in molecular dynamics simulations via massive parallelism. *J. Mater. Chem.* **16**, 1911 (2006).
56. Todorov, I. T. & Smith, W. The DL\_POLY\_4 User Manual, Version 4.06, (STFC Daresbury laboratory, Daresbury, Warrington WA4 4AD Cheshire, UK, 2014).

## Acknowledgements

This work is financially supported by the National Key Research and Development Program (No. 2019YFA0210600), the National Natural Science Foundation of China (No. 21905085; No. 51972107), and the Innovative Research Groups of Hunan Province (No. 2019JJ10001).

## Author contributions

X.L. conceived and designed the study. Y.P.Z. directed the study and contributed synthesis, battery/electrode tests. Z.X.L., L.J.G., and Q.J.D. conducted Raman and UV-vis spectroscopy studies. T.T.L., X.Z., and L.Z. performed zinc electrodeposition and SEM studies. Y.Y.L., H.B.Y., and Y.P.Z. conducted MD simulations. Y.P.Z. and X.L. contributed to data interpretation and analysis, and wrote the manuscript. All authors contributed to the scientific discussion.

## Competing interests

The authors declare no competing interests.

## Additional information


**Supplementary information** is available for this paper at <https://doi.org/10.1038/s41467-020-20331-9>.

**Correspondence** and requests for materials should be addressed to X.L.

**Peer review information** *Nature Communications* thanks the anonymous reviewers for their contribution to the peer review of this work.

**Reprints and permission information** is available at <http://www.nature.com/reprints>

**Publisher's note** Springer Nature remains neutral with regard to jurisdictional claims in published maps and institutional affiliations.

 **Open Access** This article is licensed under a Creative Commons Attribution 4.0 International License, which permits use, sharing, adaptation, distribution and reproduction in any medium or format, as long as you give appropriate credit to the original author(s) and the source, provide a link to the Creative Commons license, and indicate if changes were made. The images or other third party material in this article are included in the article's Creative Commons license, unless indicated otherwise in a credit line to the material. If material is not included in the article's Creative Commons license and your intended use is not permitted by statutory regulation or exceeds the permitted use, you will need to obtain permission directly from the copyright holder. To view a copy of this license, visit <http://creativecommons.org/licenses/by/4.0/>.

© The Author(s) 2021